Boundary Modes from Periodic Magnetic and Pseudomagnetic Fields in Graphene

Võ Tiến Phong and E. J. Mele*
Department of Physics and Astronomy, University of Pennsylvania, Philadelphia, Pennsylvania 19104, USA

(Received 13 August 2021; revised 10 December 2021; accepted 20 March 2022; published 29 April 2022)

Single-layer graphene subject to periodic lateral strains is an artificial crystal that can support boundary spectra with an intrinsic polarity. This is analyzed by comparing the effects of periodic magnetic fields and strain-induced pseudomagnetic fields that, respectively, break and preserve time-reversal symmetry. In the former case, a Chern classification of the superlattice minibands with zero total magnetic flux enforces *single* counterpropagating modes traversing each bulk gap on opposite boundaries of a nanoribbon. For the pseudomagnetic field, pairs of counterpropagating modes migrate to the *same* boundary where they provide well-developed valley-helical transport channels on a single zigzag edge. We discuss possible schemes for implementing this situation and their experimental signatures.

DOI: 10.1103/PhysRevLett.128.176406

Atomically thin materials are versatile platforms for creating new artificial crystals defined by imposing laterally periodic potentials. A celebrated example is twisted bilayer graphene where a small interlayer twist modulates the atomic registry on large moiré scales $L \sim 10$–20 nm and yields structurally tunable superperiodic solids with flattened minibands [1,2]. When the bandwidth is made much smaller than the energy gaps separating manifolds, the electronic physics projected into the spectrally isolated minibands can be controlled by various many-body effects [3,4]. Fractured spectra can be produced even for a monolayer material by other mechanisms that introduce Bragg reflections on a superlattice, such as by periodic patterning of an electrostatic gate or a perpendicular magnetic field [5,6]. The latter situation is interesting since even if the spatially averaged flux vanishes, the applied magnetic field breaks time-reversal symmetry $\mathcal{T}$, and can generate gapped minibands with nonzero Chern numbers [7,8]. However, experimentally realizing the anomalous Hall effect via this route is daunting because of the large magnetic fields required to produce sufficiently large minigaps. Nonetheless, it suggests an alternate approach where instead a periodic strain field in monolayer graphene is coupled to electronic motion and masquerades as a valley-antisymmetric pseudomagnetic field on a much larger energy scale. This has been demonstrated experimentally for a sheet of graphene contacted with $NbSe_2$ [9]. The properties of nearly flat bands in this system have been probed for possible correlated-electron physics [9–13].

Pseudomagnetic fields induce fascinating electronic phenomena even at the single-particle level associated with the symmetries of the superlattice minigaps [14–21]. Unlike a real magnetic field, the pseudofield is $\mathcal{T}$ symmetric and changes its sign in two momentum-space valleys. Each valley can host nontrivial Chern minibands, but this is exactly compensated in the time-reversed valley. Naively, one might expect this to exclude any interesting structure in the boundary spectra. However, we find that this setup still supports rich edge-state physics in its boundary spectra without topological protection [22]. Robust transport in edge channels *on selected boundaries* is generically produced by a competition between bulk and surface symmetries when such an artificial crystal is terminated. Below, we analyze the resulting edge modes, demonstrate how they produce an intrinsic polarity on a generic terminated superlattice, and suggest how these features can be probed in transport and spectroscopic measurements.

Before analyzing the band structure of monolayer graphene in a periodic strain field, we begin by considering the closely related system of *spinless* electrons in a *real* but periodic magnetic field. In this case, the superlattice bands admit a Chern topological classification even without requiring valley projection. Consequently, this allows us to identify robust edge modes that cannot be gapped out by intervalley coupling. We choose a real magnetic field that is spatially varying with a periodic profile and zero total flux, $\mathbf{B}(\mathbf{r}) = B_0\hat{z}\sum_{i=1}^{3}\cos(\mathbf{G}_i \cdot \mathbf{r})$, where $\mathbf{G}_i$ are the superlattice primitive reciprocal lattice vectors specified in Fig. 1(b). For simplicity, the superlattice translation vectors, $\mathbf{L}_i = N\mathbf{a}_i$, are chosen to be commensurate with the graphene translation vectors, $\mathbf{a}_i$, for some integer N.

In the presence of a periodic potential, the microscopic Brillouin zone (BZ) folds back to a smaller superlattice Brillouin zone (sBZ). For small N, there are two classes of structures: if $\mathrm{mod}(N, 3) = 0$, K_+ and K_- are mapped to $\bar{\Gamma}$, and otherwise, K_+ and K_- are mapped to different points. For large N, it becomes impractical to distinguish between these two classes of structures because of an emergent valley symmetry that allows us to approximately label states by a valley index. In this limit, we obtain a series of

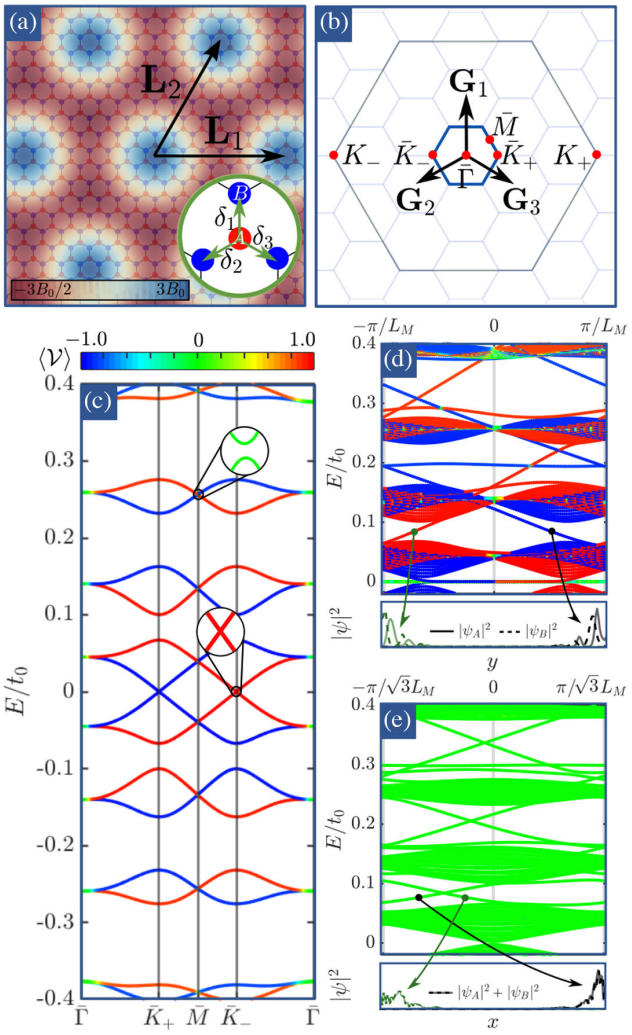

FIG. 1. Graphene in a periodically modulated magnetic field. (a) Real-space and (b) reciprocal-space representations of graphene in a periodic magnetic field. (c) Band structure for $N = 14$ and $\delta t = 0.3$. The energy eigenstates are color coded by their valley expectation value $\langle\mathcal{V}\rangle$ as in Ref. [11]. We observe that the bands close to $E = 0$ are exceptionally well valley polarized. Within each valley, there is a doublet band at $E = 0$, and singlet bands elsewhere. Band structures on a finite zigzag (d) and armchair (e) nanoribbon showing protected topological edge states at every insulating gap shown. In the zigzag configuration, we see that the edge states are highly valley polarized. Electron density distributions for some representation edge states are shown below each band structure. Here, each ribbon has 175 carbon atoms across its width.

isolated flat bands near charge neutrality. Within a single valley, there is one two-dimensional manifold that crosses $E = 0$, and one-dimensional manifolds elsewhere near $E = 0$. We use $N = 14$ for efficient numerical calculations throughout this work, though conclusions reached here are applicable to other cases of larger N as well. A representative band structure in this limit for $N = 14$ is shown in Fig. 1(c). To characterize the band topology of this $\mathcal{T}$-broken system, we calculate the Chern number associated with every insulating gap close to charge neutrality numerically using a finite difference method [23,24]. In our case, since the gaps induced by intervalley hybridization are quite small, a sufficiently fine $\mathbf{k}$-space mesh is necessary in order to obtain convergent results. We find that all the insulating bulk gaps near charge neutrality carry $\mathcal{C} = \mathrm{sign}(B_0 E)$.

The presence of a nonzero Chern number requires the existence of a dispersive band in the bulk gap at every boundary termination for a macroscopic sample. In an armchair termination, K_+ and K_- are mapped onto the same wave vector of the ribbon Hamiltonian, so we do not expect edge modes to carry definite valley character. In a zigzag termination, K_+ and K_- are well separated in the boundary-projected crystal momentum. Consequently, we expect edge modes in this case to be valley polarized close to charge neutrality. This is confirmed numerically, as shown in Figs. 1(d) and 1(e). Interestingly, because $\mathcal{C} = \pm 1$ for *all* the relevant insulating gaps, there is only *one* topological edge mode per boundary in each bulk gap. The boundary states in a zigzag nanoribbon from different valleys belong to opposite edges. This situation is very similar to the edge modes associated with the famous $n = 0$ Landau level of a Dirac Hamiltonian where each valley contributes an edge state at a different edge [25,26]. However, the present system with a periodic magnetic field is distinct from the Landau-level scenario because of the absence of prominent insulating gaps with higher Chern numbers. In the Landau-level problem, each band carries a nonzero Chern number, and the number of edge modes thus increases in the higher gaps. The valley-polarized edge states associated with these higher-Chern-number Landau-level gaps occur on both boundaries of a zigzag nanoribbon.

Using the insights from studying a periodic magnetic field, we now examine graphene under a periodic strain field. Under such a field, the bond strengths between carbon atoms are periodically modulated in space. Again, in the limit $N \gg 1$, we expect *emergent* superlattice-scale symmetries to dominate the low-energy physics. For a sufficiently smooth superlattice potential, it is useful to approximate the physics near charge neutrality by considering *independent* valley Dirac fermions at K_+ and K_-. Throughout this Letter, we neglect the scalar contribution of the strain field by assuming that only nearest-neighbor hoppings are significant and the substrate is chemically and electronically inert [27]. In this theory, the strain field enters the Hamiltonian as a spatially dependent pseudogauge field. Inspired by a recent experiment [9], we choose the pseudomagnetic field to be the same as before in one of the valleys, $\mathbf{B}_\nu(\mathbf{r}) = \nu B_0 \hat{z} \sum_{i=1}^{3} \cos(\mathbf{G}_i \cdot \mathbf{r})$, where $\nu = \pm$ denotes valleys. The valley-projected, long-wavelength Hamiltonian is

$$\hat{\mathcal{H}}_\nu = \hbar v_F \int d^2\mathbf{r} \hat{\psi}^\dagger(\mathbf{r}) \left(-i\nabla_\mathbf{r} + \frac{e}{\hbar} \mathbf{A}_\nu(\mathbf{r}) \right) \cdot (\nu\sigma_x, \sigma_y) \hat{\psi}(\mathbf{r}), \tag{1}$$

where $\hat{\psi}^\dagger(\mathbf{r}) = (\hat{\psi}_A^\dagger(\mathbf{r}), \hat{\psi}_B^\dagger(\mathbf{r}))$ are the sublattice creation operators and σ_j act on the sublattice degrees of freedom. In our convention, the charge q is $q = -e$. Under a gauge transformation $\mathbf{A}_\nu(\mathbf{r}) \mapsto \mathbf{A}_\nu(\mathbf{r}) - \nabla f(\mathbf{r})$, the wave functions simply acquire a local U(1) phase $\psi(\mathbf{r}) \mapsto \exp(ief(\mathbf{r})/\hbar)\psi(\mathbf{r})$. This valley-projected Hamiltonian is invariant under the magnetic point symmetry group $3\underline{m}$, with three classes $\{E, C_{3z}, \mathcal{T}M_x\}$ [28,33,34]. When both valleys are considered, then the full Hamiltonian respects C_{3z}, M_x, and $\mathcal{T}$. Importantly, C_{2z} is broken in this configuration.

Just as in the case of a real magnetic field, the presence of a periodic potential produced by strain fractures the energy spectrum into a series of narrow bands. In the limit of exact valley symmetry, we learn from the case of a real magnetic field that each valley contributes a single edge mode at the insulating gaps away from $E = 0$ on a particular boundary of a zigzag nanoribbon. If valley mixing is prohibited, these edge modes must also exist in graphene under a periodic strain. However, due to $\mathcal{T}$ symmetry, the two edge modes coming from both valleys now must populate the *same* zigzag boundary. In other words, the sign change of the pseudomagnetic field between valleys is realized by having the edge states reside on only *one side* of a zigzag nanoribbon. Of course, valley symmetry is not strictly exact in a microscopic theory. However, one can effectively suppress intervalley scattering by increasing the superlattice period and operating in the ballistic limit, both of which are achievable in graphene-based platforms. For these reasons, we expect these edge modes to be robust and allow their experimental detection and manipulation although they are not topologically protected.

To confirm the existence of these boundary states numerically, we construct a tight-binding representation of Hamiltonian (1) which respects all of the aforementioned symmetries. Practically, the exact strain field is seldom determined in an experiment. So we use a desired pseudomagnetic field as the starting point and find a suitable corresponding tight-binding parametrization. To do so, we employ the following approximation $ev_F[A_x(\mathbf{R}_j) + iA_y(\mathbf{R}_j)] \approx -\sum_{i=1}^{3} \delta t_i(\mathbf{R}_j) e^{-i\mathbf{K}_+\cdot\boldsymbol{\delta}_i}$, where $\delta t_i(\mathbf{R}_j)$ is the bond strength modulation along the $\boldsymbol{\delta}_i$ direction as shown in Fig. 1(a) [35–37]. Among the many possible choices for $\delta t_i(\mathbf{R}_j)$, we adopt the following gauge that respects all the spatial symmetries of the continuum model, $\delta t_i(\mathbf{R}_j) = t_0\delta t \sin(\mathbf{G}_i \cdot \mathbf{R}_j)$, where $t_0\delta t = \sqrt{3}v_F eB_0 L/4\pi$ [11,12]. A realization in this gauge is shown in Fig. 2(a), where it is immediately clear that C_{3z} and M_x are preserved. Importantly, C_{2z} is broken explicitly. If it were preserved, the accumulation of edge modes on only one edge would be impossible when the edge termination is C_{2z} symmetric. This would render the existence of the boundary-selective edge modes dependent on the precise width of a zigzag nanoribbon.

At low energies, we have confirmed numerically that the bands calculated from the continuum model qualitatively

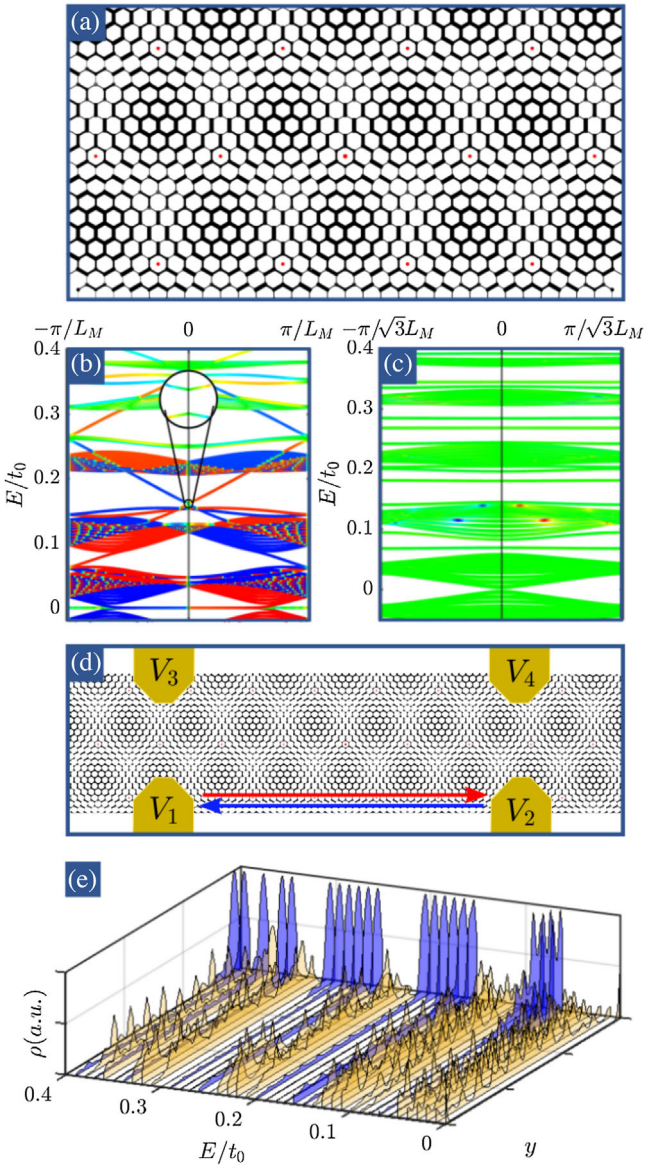

FIG. 2. Graphene in the presence of a periodic strain. (a) Lattice realization of the gauge field defined in the text with the bond strength indicated by the thickness of the bonds. In this gauge, C_{3z} and M_x are evidently preserved. Band structures on a finite zigzag (b) nanoribbon showing edge states at every insulating gap. These edge states sometimes meet at $\mathcal{T}$-invariant momenta and form small avoided crossings. There are no corresponding edge modes in the armchair configuration (c). The bands are colored according to their valley character, as detailed in Fig. 1. Here, $N = 14$, $\delta t = 0.3$, and each ribbon has 175 carbon atoms across its width. (d) A four-terminal setup to measure the existence of the one-sided boundary states when the chemical potential resides within one of the bulk gaps. When a potential difference is applied across V_1 and V_2, a current flows across the two terminals. On the other hand, when a potential difference is applied across V_3 and V_4, no current is detected. (e) Local density of states as a function of energy E and position y. The midgap states shown in blue are localized to only one edge. The bulk states shown in yellow are extended throughout the sample. For this simulation, the ribbon has 150 carbon atoms across its width.

match those produced by the tight-binding model. We then diagonalize the Hamiltonian on finite ribbons with zigzag and armchair terminations. Indeed, in the zigzag configuration where intervalley scattering is suppressed, we find edge states residing in the insulating gaps away from charge neutrality, as shown in Fig. 2(b). The branches from opposite valleys have small avoided crossings at $\mathcal{T}$-invariant momenta. These one-sided boundary states can be detected in a transport measurement using a four-terminal setup as shown in Fig. 2(d): when the chemical potential is in a bulk gap, one of the two edges acts as an insulator while the other is a conductor. Because of this, while the phase with a real magnetic field is characterized by quantized Hall conductivity, this time-reversal symmetric phase necessarily has zero Hall conductivity, but carries quantized longitudinal conductance on the active edge in the clean limit. Another possible detection is by measuring the edge asymmetry in the local density of states (LDOS). Within each of the bulk gaps, the LDOS will be strongly enhanced on only one side of a zigzag sample for almost all energies throughout that gap, as shown in Fig. 2(e). This surface charge accumulation to one side of the sample is evidence that the zigzag termination generates a polarity in a macroscopic sample with open boundary conditions. We note that there are no corresponding edge modes for the special case of an armchair configuration due to significant valley mixing, as shown in Fig. 2(c).

Having established the presence of edge modes on one side of a zigzag nanoribbon, we now explore different strain profiles which can give rise to the appropriate effective pseudomagnetic field for these edge modes to be observed [38]. As a first example, let us consider a strained flat sheet with $h = 0$. Periodic strain fields without vertical displacements must be accompanied by periodically-embedding regions of local compression ($\nabla \cdot \mathbf{u} < 0$) and extension ($\nabla \cdot \mathbf{u} > 0$). One example strain field of this type is $u_x \propto \sqrt{3}\cos(\mathbf{G}_2 \cdot \mathbf{r}) - \sqrt{3}\cos(\mathbf{G}_3 \cdot \mathbf{r})$ and $u_y \propto \cos(\mathbf{G}_2 \cdot \mathbf{r}) + \cos(\mathbf{G}_3 \cdot \mathbf{r}) - 2\cos(\mathbf{G}_1 \cdot \mathbf{r})$. We notice that this strain field preserves C_{3z} and breaks C_{2z} as required. However, while flat strain fields contain all the necessary theoretical ingredients to produce the desired effect, they would not be easily achievable because of the large elastic-energy cost incurred as a result of the inevitable local compressive strain.

We can alternatively obtain the desired pseudogauge field by lifting the model into the third dimension and imposing an appropriate height profile $h(\mathbf{r})$. This approach offers more experimental control because the height profile can be engineered simply by placing graphene on a substrate designed to produce a desired height profile $h(\mathbf{r})$. As the graphene membrane conforms to the substrate topography, it deforms not only vertically but laterally as well to minimize elastic energy. Taking into account relaxation in all three directions [39,40], the following height profiles produce the desired pseudogauge fields,

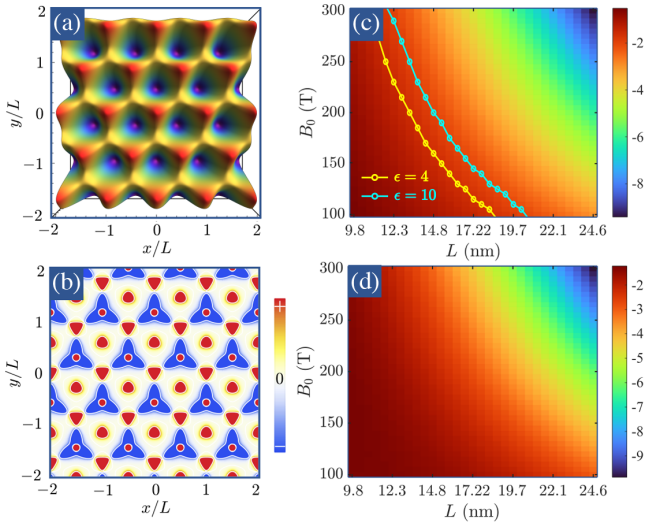

FIG. 3. Designing strain fields. (a) $h(\mathbf{r})$ and (b) its Gaussian curvature with $\phi = -\pi/4$ as defined in the text. Following Ref. [10], we show (c) the estimated bandwidth of the energy manifold at charge neutrality and (d) the estimated magnitude of the first insulating gap above charge neutrality. The yellow and cyan lines show the Coulomb energy scale $E \sim 14.4\ \text{Å eV}/\epsilon L$ for $\epsilon = 4$ and $\epsilon = 10$, respectively. The color maps have units $\log_{10}$ (eV).

$h(\mathbf{r}) = h_0 \sum_{i=1}^{3} \cos(\mathbf{G}_i \cdot \mathbf{r} + \phi)$ with $\phi = \pm\pi/4$. Roughly, this profile can be created in two ways: either by arranging *triangular* pillars on a triangular lattice or by placing *cylindrical* pillars in a hexagonal lattice where the heights of the two sublattices are different, as shown in Fig. 3(a). The plus (+) and minus (−) signs on ϕ indicate two complementary structures with opposite orientations, one features boundary states on the top edge and the other on the bottom edge. These two structures cannot be locally transformed into one another. This can be understood in terms of the Gaussian curvature. The local Gaussian curvature for $\phi = -\pi/4$ is shown in Fig. 3(b). To get the complementary structure, we need to invert the local Gaussian curvature at various high-symmetry regions of the unit supercell. However, since the total curvature over one unit supercell is always zero due to the Gauss-Bonnet theorem, this can only be done by a global transformation of the structure that interchanges extrema and saddle points in the height profile. We note that since the Gaussian curvature is invariant under the reflection $h \mapsto -h$, inverting the sign of the vertical deflection does not transform to a complementary structure. The pseudomagnetic field produced by this strain field has magnitude $B_0 \sim (6 \times 10^5) \times h_0^2/N^3\ \text{T/Å}^2$. Using Figs. 3(c) and 3(d) as a guide, h_0 can be chosen for a given N to yield the desired bandwidths and gaps. For instance, for $N = 60$ and $B_0 = 100$ T, we find $h_0 \approx 6$ Å.

The preceding considerations show that in addition to the recently-realized platform using $NbSe_2$, the edge-state

physics we uncover here should be accessible in many other graphene-based settings with appropriately engineered substrate topographies. Namely, strain fields that break C_{2z} can produce one-sided edge states. Actually, similar physics can be accessed using nonperiodic strains as well, as described in Ref. [22]. We emphasize that while these edge states are fragile near avoided crossings in the presence of valley mixing, we can exponentially suppress intervalley hybridization by increasing the superlattice period. Furthermore, disorder can of course lead to localization just as in the case of topological crystalline insulators where disorder generically breaks the spatial symmetries needed to protect edge states [41,42]. However, if disorder on average preserves valley symmetry, it is reasonable to expect these edge modes will persist as high-mobility transport channels [42,43]. In this limit, we can still regard valley as a good approximate quantum number. This strong valley-helical character of these edge modes is of intrinsic technological interest since it can potentially be harnessed for various valleytronic applications [44–46]. Finally, it is worth considering in future works the possibility that the boundary physics explored here might be accessible in other two-dimensional materials as well.

We thank Antonio L. R. Manesco, Eva Andrei, Francisco Guinea, and Martin Claassen for useful discussions. V. T. P. acknowledges support from the NSF Graduate Research Fellowships Program and the P. D. Soros Fellowship for New Americans. E. J. M. is supported by the Department of Energy under Grant No. DE-FG02-84ER45118.

*mele@physics.upenn.edu

[1] Y. Cao, V. Fatemi, A. Demir, S. Fang, S. L. Tomarken, J. Y. Luo, J. D. Sanchez-Yamagishi, K. Watanabe, T. Taniguchi, E. Kaxiras *et al.*, Correlated insulator behaviour at half-filling in magic-angle graphene superlattices, Nature (London) **556**, 80 (2018).

[2] Y. Cao, V. Fatemi, S. Fang, K. Watanabe, T. Taniguchi, E. Kaxiras, and P. Jarillo-Herrero, Unconventional superconductivity in magic-angle graphene superlattices, Nature (London) **556**, 43 (2018).

[3] E. Y. Andrei and A. H. MacDonald, Graphene bilayers with a twist, Nat. Mater. **19**, 1265 (2020).

[4] L. Balents, C. R. Dean, D. K. Efetov, and A. F. Young, Superconductivity and strong correlations in moiré flat bands, Nat. Phys. **16**, 725 (2020).

[5] R. Brown, Electronic properties of graphene superlattices: Transport and superconductivity, Ph.D. thesis, University of Manchester, 2020.

[6] A. Skurativska, S. S. Tsirkin, F. D. Natterer, T. Neupert, and M. H. Fischer, Flat bands with fragile topology through superlattice engineering on single-layer graphene, Phys. Rev. Research **3**, L032003 (2021).

[7] D. J. Thouless, M. Kohmoto, M. P. Nightingale, and M. den Nijs, Quantized Hall Conductance in a Two-Dimensional Periodic Potential, Phys. Rev. Lett. **49**, 405 (1982).

[8] F. D. M. Haldane, Model for a Quantum Hall Effect Without Landau Levels: Condensed-Matter Realization of the "Parity Anomaly", Phys. Rev. Lett. **61**, 2015 (1988).

[9] J. Mao, S. P. Milovanović, M. Anđelković, X. Lai, Y. Cao, K. Watanabe, T. Taniguchi, L. Covaci, F. M. Peeters, A. K. Geim *et al.*, Evidence of flat bands and correlated states in buckled graphene superlattices, Nature (London) **584**, 215 (2020).

[10] S. P. Milovanović, M. Anđelković, L. Covaci, and F. M. Peeters, Band flattening in buckled monolayer graphene, Phys. Rev. B **102**, 245427 (2020).

[11] A. L. Manesco, J. L. Lado, E. V. Ribeiro, G. Weber, and D. Rodrigues Jr, Correlations in the elastic landau level of spontaneously buckled graphene, 2D Mater. **8**, 015011 (2021).

[12] A. L. R. Manesco and J. Lado, Correlation-induced valley topology in buckled graphene superlattices, 2D Mater. **8**, 035057 (2021).

[13] D. Giambastiani, F. Colangelo, A. Tredicucci, S. Roddaro, and A. Pitanti, Electron localization in periodically strained graphene, J. Appl. Phys. **131**, 085103 (2022).

[14] A. H. Castro Neto, F. Guinea, N. M. R. Peres, K. S. Novoselov, and A. K. Geim, The electronic properties of graphene, Rev. Mod. Phys. **81**, 109 (2009).

[15] N. Levy, S. Burke, K. Meaker, M. Panlasigui, A. Zettl, F. Guinea, A. C. Neto, and M. F. Crommie, Strain-induced pseudo–magnetic fields greater than 300 tesla in graphene nanobubbles, Science **329**, 544 (2010).

[16] F. Guinea, M. Katsnelson, and A. Geim, Energy gaps and a zero-field quantum hall effect in graphene by strain engineering, Nat. Phys. **6**, 30 (2010).

[17] G. G. Naumis and P. Roman-Taboada, Mapping of strained graphene into one-dimensional hamiltonians: Quasicrystals and modulated crystals, Phys. Rev. B **89**, 241404 (2014).

[18] P. Roman-Taboada and G. G. Naumis, Topological phase-diagram of time-periodically rippled zigzag graphene nanoribbons, J. Phys. Commun. **1**, 055023 (2017).

[19] C. Si, Z. Sun, and F. Liu, Strain engineering of graphene: A review, Nanoscale **8**, 3207 (2016).

[20] M. T. Mahmud and N. Sandler, Emergence of strain-induced moiré patterns and pseudomagnetic field confined states in graphene, Phys. Rev. B **102**, 235410 (2020).

[21] R. Banerjee, V.-H. Nguyen, T. Granzier-Nakajima, L. Pabbi, A. Lherbier, A. R. Binion, J.-C. Charlier, M. Terrones, and E. W. Hudson, Strain modulated superlattices in graphene, Nano Lett. **20**, 3113 (2020).

[22] T. Low and F. Guinea, Strain-induced pseudomagnetic field for novel graphene electronics, Nano Lett. **10**, 3551 (2010).

[23] T. Fukui, Y. Hatsugai, and H. Suzuki, Chern numbers in discretized brillouin zone: Efficient method of computing (spin) hall conductances, J. Phys. Soc. Jpn. **74**, 1674 (2005).

[24] D. Vanderbilt, *Berry Phases in Electronic Structure Theory: Electric Polarization, Orbital Magnetization and Topological Insulators* (Cambridge University Press, Cambridge, England, 2018).

[25] L. Brey and H. A. Fertig, Edge states and the quantized hall effect in graphene, Phys. Rev. B **73**, 195408 (2006).

[26] D. A. Abanin, P. A. Lee, and L. S. Levitov, Spin-Filtered Edge States and Quantum Hall Effect in Graphene, Phys. Rev. Lett. **96**, 176803 (2006).

[27] R. Brown, N. R. Walet, and F. Guinea, Edge Modes and Nonlocal Conductance in Graphene Superlattices, Phys. Rev. Lett. **120**, 026802 (2018).
[28] See Supplemental Material at http://link.aps.org/supplemental/10.1103/PhysRevLett.128.176406, which includes Refs. [29–32].
[29] H. Suzuura and T. Ando, Phonons and electron-phonon scattering in carbon nanotubes, Phys. Rev. B **65**, 235412 (2002).
[30] J. L. Mañes, Symmetry-based approach to electron-phonon interactions in graphene, Phys. Rev. B **76**, 045430 (2007).
[31] F. de Juan, J. L. Mañes, and M. A. H. Vozmediano, Gauge fields from strain in graphene, Phys. Rev. B **87**, 165131 (2013).
[32] Z. Song, Z. Wang, W. Shi, G. Li, C. Fang, and B. A. Bernevig, All Magic Angles in Twisted Bilayer Graphene are Topological, Phys. Rev. Lett. **123**, 036401 (2019).
[33] M. Tinkham, *Group Theory and Quantum Mechanics* (Courier Corporation, Mineola, New York, 2003).
[34] M. S. Dresselhaus, G. Dresselhaus, and A. Jorio, *Group Theory: Application to the Physics of Condensed Matter* (Springer, Berlin, Heidelberg, 2007).
[35] E.-A. Kim and A. C. Neto, Graphene as an electronic membrane, Europhys. Lett. **84**, 57007 (2008).
[36] V. M. Pereira and A. H. Castro Neto, Strain Engineering of Graphene's Electronic Structure, Phys. Rev. Lett. **103**, 046801 (2009).
[37] M. R. Masir, D. Moldovan, and F. Peeters, Pseudo magnetic field in strained graphene: Revisited, Solid State Commun. **175**, 76 (2013).
[38] M. A. Vozmediano, M. Katsnelson, and F. Guinea, Gauge fields in graphene, Phys. Rep. **496**, 109 (2010).
[39] F. Guinea, B. Horovitz, and P. Le Doussal, Gauge field induced by ripples in graphene, Phys. Rev. B **77**, 205421 (2008).
[40] T. Wehling, A. Balatsky, A. Tsvelik, M. Katsnelson, and A. Lichtenstein, Midgap states in corrugated graphene: *Ab initio* calculations and effective field theory, Europhys. Lett. **84**, 17003 (2008).
[41] L. Fu, Topological Crystalline Insulators, Phys. Rev. Lett. **106**, 106802 (2011).
[42] Y. Ando and L. Fu, Topological crystalline insulators and topological superconductors: From concepts to materials, Annu. Rev. Condens. Matter Phys. **6**, 361 (2015).
[43] I. Mondragon-Shem and T. L. Hughes, Robust topological invariants of topological crystalline phases in the presence of impurities, arXiv:1906.11847.
[44] S. Milovanović and F. Peeters, Strain controlled valley filtering in multi-terminal graphene structures, Appl. Phys. Lett. **109**, 203108 (2016).
[45] J. R. Schaibley, H. Yu, G. Clark, P. Rivera, J. S. Ross, K. L. Seyler, W. Yao, and X. Xu, Valleytronics in 2d materials, Nat. Rev. Mater. **1**, 16055 (2016).
[46] S. A. Vitale, D. Nezich, J. O. Varghese, P. Kim, N. Gedik, P. Jarillo-Herrero, D. Xiao, and M. Rothschild, Valleytronics: Opportunities, challenges, and paths forward, Small **14**, 1801483 (2018).